Design and Control of a Two-Degree-of-Freedom Lightweight Flexible Arm

Vicente Feliu[1], H. Benjamin Brown, Jr., and Kuldip S. Rattan[2]

CMU-RI-TR-89-21

The Robotics Institute
Carnegie Mellon University
Pittsburgh, Pennsylvania 15213

July 1989

[1] Visiting Professor, Dpto Ingenieria Electrica, Electronica y Control, UNED, Ciudad Universitaria, Madrid 28040, Spain.

[2] Visiting Professor, Department of Electrical Systems Engineering, Wright State University, Dayton, OH 45435

Table of Contents

List of Figures

Abstract

This report describes the design and control of a two-joint, two-link flexible arm. Our purpose has been to build an efficient arm in the sense that most of the energy provided by the motors is spent in doing the task (moving the tip mass) instead of moving the arm structure. In order to achieve that, we designed a flexible arm that has most of its mass concentrated on the tip. We wanted also to decouple radial tip motions from angular tip motions. The special mechanical configuration that fulfills all these specifications is described in Section 2.

Section 3 describes the control scheme of this arm. An important problem when controlling it was the large Coulomb friction of the motors. A two-nested-loop multivariable controller has been used. The inner loop controls the position of the motors while the outer loop controls the tip position. The resolved acceleration method is generalized to control this flexible arm. The compliance matrix was used to model the oscillations of the structure, and was included in the decoupling/linearizing term of this controller. Experimental results are given in Section 4, and conclusions are drawn in Section 5.

1. Introduction

This report describes the design and control of a small two-joint, two-link flexible arm that we have built in our laboratory. This arm operates in a plane on an air table. The arm is designed with exaggerated flexibility to facilitate studying the control of flexible structures; and is very light in weight compared to the mass placed at the tip (there is no mass placed at the elbow joint).

The purpose of our research on flexible arms is to design more efficient and faster arms than the actual rigid arms. Our very lightweight arm is efficient in the sense that most of the energy provided by the motors is spent in doing the task (moving the tip mass), and little is wasted in moving the arm structure (unlike rigid arms).

We wanted also to decouple radial motions of the tip from angular motions. A special four-bar linkage is used to drive the elbow joint from a motor mounted near the base. Mechanics of this arm are described in Section 2; and a dynamical model is developed for this arm, that can be easily extended to any n-degrees of freedom lumped-mass flexible arm.

Section 3 describes the control scheme of this arm. An important problem when controlling it was the large Coulomb friction of the motors. A two-nested-loop controller has been used. The inner loop controls the position of the motors while the outer loop controls the tip position. This method is the generalization to robots with more than one degree of freedom of the control method described in [1],[2],[3], which is very robust to changes in the dynamic friction and insensitive to the Coulomb friction.

A generalization of the resolved acceleration method ([4], a.e.) to the case of flexible arms is implemented in the outer loop. The compliance matrix was used to model the oscillations of the structure, and was included in the decoupling/linearizing term of this controller. Experimental results are given in Section 4, and conclusions are drawn in Section 5.

2. Mechanical issues

This arm has been designed to fulfill two specifications, from the mechanical point of view:

1. the arm had to be very lightweight,
2. radial motions of the tip had to be nearly decoupled from angular motions (if we neglect the vibrations because of flexibility).

In order to fulfill the first specification, the links were made of a very lightweight wire (having consequently a significant elasticity), and the motor that moves the elbow was placed close to the base of the arm. A four-bar linkage was used to transmit the motion of this motor to the elbow.

In order to fulfill the second specification, the length of the two links was made the same, and the dimensions of the four-bar linkage were especially designed.

Subsections 2.1. and 2.2. study the kinematics and dynamics of this arm assuming that is rigid. Subsection 2.3. includes the flexibility effects.

2.1. Kinematics

Figure 1 illustrates the kinematics of the arm, neglecting its compliance. The arm comprises a four-bar linkage with pivots at points O, A, B and C, and tip position, P. Note that the length of link $O-A$ is twice that of link $B-C$; and links $O-C$ and $C-P$ are of equal length. With points O and A fixed, as shown (for the sake of studying kinematic behavior–A is not normally fixed), it can be shown that the tip describes a path very close to a straight line through the origin (O) at an angle of 45 degrees to the x-axis. That is, as the radius to the tip (ρ) varies, the tip angle (γ) remains close to 45 degrees (γ_0). The point P_0 is the ideal tip position, assuming that

$$\rho = \rho_0 = 2 \cdot l \cdot \cos(\varphi - 45). \tag{1}$$

Analysis of the geometry reveals that the error (deviation from ideal) in the tip angle is given by

$$\epsilon_\gamma \approx \epsilon/2 \tag{2}$$

and the error in tip radius by

$$\epsilon_\rho = \frac{e_\rho}{2 \cdot l} \approx \epsilon \cdot \frac{\sin(\varphi) - \cos(\varphi)}{2 \cdot \sqrt{2}}, \tag{3}$$

where e_ρ is the radial error, ϵ_ρ is the normalized radial error,

$$\epsilon = \frac{2 \cdot (\alpha + \cos(\varphi)) \cdot (1 - \sin(\varphi))}{1 - 2 \cdot (\alpha + \cos(\varphi)) \cdot \cos(\varphi)}, \tag{4}$$

and

$$\alpha = a/l. \tag{5}$$

Figure 2 gives the normalized errors as functions of the normalized tip radius ($\rho/(2 \cdot l)$) for several values of parameter α (a/l). The value $\rho/(2 \cdot l)$ represents the percentage of arm extension, and has a maximum range of $0 - 1.0$. For a typical value of α, say 0.2, we see from the plot that the deviations are quite small ($< 1\%$) in the range of $.4 < \rho/(2 \cdot l) < .8$; and less than 5 % in the range $.25 < \rho/(2 \cdot l) < .9$. By restricting the range of motion of the arm, then, we can minimize the deviation from ideal behavior. While the deviation will require consideration for precise tip positioning, that is in the kinematic calculations, the effects can be ignored with regard to system dynamics. This can simplify dynamic calculations substantially.

This kinematic design provides a means for decoupling the two joint actuators. We mount one of the actuators so that it drives link $O-A$ with respect to ground (see Figure 3). The net effect of a torque

from this actuator is a tangential force at the tip. We mount the second actuator so that it drives link $O-C$ with respect to link $O-A$. Thus, it generates equal and opposite torques on the two links; the net effect is a radial force at the tip. In terms of position control, a displacement of the first actuator generates a pure tangential motion; of the second, a pure radial motion. The decoupling effects are based on the ideal (straight-line) behavior of the arm; there will be some deviation from this fully decoupled behavior, especially near the extremes of travel ($\rho = 0, \rho = 1$) of the arm. One consequence of this geometry is that there is no torque coupling between actuators: a torque at one actuator generates no reaction torque at the other. This simplifies control, and possibly reduces energy usage of the arm.

2.2. Rigid arm dynamics

We develop in this subsection the dynamics of this arm assuming that is rigid. We will complete this model in the next subsection, adding the effects of the link compliance.

Using Lagrange equations (or Newton-Euler equations) we get:

$$\begin{pmatrix} F_\rho \\ F_\gamma \end{pmatrix} = m \cdot \left(\begin{pmatrix} \ddot{\rho} \\ \rho \cdot \ddot{\gamma} \end{pmatrix} + \begin{pmatrix} -\rho \cdot \dot{\gamma}^2 \\ 2 \cdot \dot{\rho} \cdot \dot{\gamma} \end{pmatrix} \right), \tag{6}$$

where F_ρ, F_γ are respectively the radial and angular forces applied to the tip, (ρ, γ) are the polar coordinates of the tip and m is the tip mass.

We have to express the above equation in terms of the torques T_1 and T_2 generated by the motors. Because of the decoupling between the two motors, and applying the principle of virtual work, the next approximate expression easily follows:

$$\begin{pmatrix} T_1 \\ T_2 \end{pmatrix} \approx \begin{pmatrix} 0 & 2 \cdot l \cdot \cos(\varphi) \\ 2 \cdot l \cdot \sin(\varphi) & 0 \end{pmatrix} \cdot \begin{pmatrix} F_\rho \\ F_\gamma \end{pmatrix}. \tag{7}$$

2.3. Compliance

For a system (2-joint, planar arm) that can be modelled as having all its mass concentrated at the tip, it is useful to think in terms of the compliance at the tip. Control of the tip mass then becomes a matter of producing deflections to generate the appropriate tip forces. This is the two-dimensional equivalent of deflecting a spring to generate a force.

It can be shown that the compliance (or stiffness) of a linear, two-dimensional system can be defined by two, orthogonal stiffness values, i.e. decoupled [5]. These principal axes of stiffness are offset by some angle from the coordinate axes of the arm. Figure 4 shows a general, planar structure (arm) connecting the tip with a fixed base. The vectors emanating from the tip indicate the magnitude and direction of the principal stifnesses. A force along either of these axes (u/v) produces a deflection parallel to the force, while a force not aligned with the axes produces a component of deflection perpendicular to the force. The general relationship between forces and displacements is given by

$$\begin{pmatrix} F_x \\ F_y \end{pmatrix} = \begin{pmatrix} k_{1,1} & k_{1,2} \\ k_{2,1} & k_{2,2} \end{pmatrix} \cdot \begin{pmatrix} \delta x \\ \delta y \end{pmatrix} \tag{8}$$

where F_x and F_y are forces applied to tip; δx and δy are tip deflections; and $k_{i,j}$ are stiffness coefficients.

We can think of the system as comprising two separate parts, as shown in Figure 5: a rigid positioner which controls the position of a cage; and inside the cage, a set of orthogonal springs, corresponding to the principal stiffnesses, that connect the cage to the tip. Thus, by appropriately positioning the cage using the arm (positioner), we can deflect the springs and generate arbitrary forces on the tip.

The question now arises as to how to find the relationship between forces and displacements, i.e. the stiffness matrix at the tip. For simple systems, these values can be calculated. For more complex systems, or for confirming analytical results, we can deduce these from observations of the natural frequencies of the mechanical system. The stiffness matrix will, of course, vary with the configuration of the arm, in particular, with the extension (ρ) of the arm. Note that we have defined the stiffness matrix with respect to coordinates $x - y$ aligned with the base-to-tip vector. We do this so that the stiffness matrix depends only on the variable ρ. Thus a coordinate rotation is needed to transform to world coordinates. For use on a digital computer, tabular storage of stiffness parameters is indicated.

The first approach involves calculating stiffness parameters for individual links, then combining these through appropriate force/moment analysis. The stiffness parameters can be defined either in terms of principal stiffness vectors (magnitude and orientation of the principal stiffnesses); or in terms of the stiffness matrix. In either case, three values are required (for any value of the extension, ρ); and these values will be referenced to the coordinate axis aligned with the base-to-tip radius vector. Performing this analysis for our particular arm with its four-bar linkage, we get the following compliance matrix C, which is the inverse of the stiffness matrix described in expression (8):

$$\begin{pmatrix} \delta x \\ \delta y \end{pmatrix} = \begin{pmatrix} c_{1,1} & c_{1,2} \\ c_{2,1} & c_{2,2} \end{pmatrix} \cdot \begin{pmatrix} F_x \\ F_y \end{pmatrix}, \tag{9}$$

where:

$$c_{1,1} = \frac{l^2 \cdot \sin^2(\varphi)}{k_c} \cdot (1 + 4 \cdot \frac{k_c}{k_b}) \tag{10}$$

$$c_{1,2} = c_{2,1} = l^2 \cdot \sin(\varphi) \cdot \cos(\varphi)/k_c \tag{11}$$

$$c_{2,2} = l^2 \cdot \cos^2(\varphi)/k_c, \tag{12}$$

and k_b, k_c are the individual stiffnesses of links $O - C$ and $C - P$ respectively. Notice that the stiffness of link $A - B$ does not appear because this link is not subjected to bending, only tension and compression.

Figure 6 plots the calculated stiffness vectors for various configurations of the experimental arm. While it may be more convenient for control purposes to store values of stiffness matrix, the vector plots

give a readily understandable picture of the stiffness characteristics. Double arrowheads in figure indicate vectors extend beyond available space.

In the second (empirical) approach to finding stiffness parameters, we excite the natural modes of vibration of the system, having known tip mass, keeping both joints angles fixed. We can do this by plucking the system and observing its time response; or by exciting with an adjustable-frequency harmonic input signal, and seeking the peak responses. Either way, we obtain the magnitudes and directions of the two principal vibration modes, which correspond to the two principal stiffnesses. The relationship between frequency and stiffness is given by

$$\omega_n = \sqrt{k/m} \tag{13}$$

where k is one principal stiffness, ω_n the corresponding frequency and m the tip mass. Using this approach, we can find values for a substantial number of configurations (values of ρ) and interpolate to get intermediate values to fill a table; or experimentally find values for only a few configurations, and use an analytical model of the system to extrapolate over the needed range. Experimental results of this approach are described later in Section 4.

The dynamic model of an n-degrees of freedom lightweight flexible arm with the mass concentrated at the tip can be represented by the scheme of Figure 7, using the stiffness/compliance matrix. This is a generalization of the dynamics of the rigid arm case (rigid arm dynamics are a block in this diagram). In this figure, $\hat{J}$ is the jacobian of the rigid arm kinematics, that relates motor velocities to tip velocities (in our particular arm, in polar coordinates); T_F is the matrix of expression (7) that transforms tip forces into motor torques; F are the tip forces; P is the tip position, and Θ_{me} are the corresponding joint coordinates (actuator coordinates) assuming that the arm is undeflected.

3. Control issues

3.1. General scheme

Our arm presents two special problems that most arms do not have: a large Coulomb friction in the joints, and flexibility in the links. They require the design of a special controller that is described in this section. We use four measurements to control this arm: a tracking camera gives the tip position in cartesian coordinates (x, y), and two potentiometers mounted on the motors give the motor position (joint angles). Because the arm has been designed in such a way that its rigid dynamics are nearly decoupled in polar coordinates, we will use these coordinates for the tip position control. Transformation to polar coordinates from cartesian measurements given by the camera is straightforward and does not introduce any error because it does not use any kinematic parameter of the arm.

In order to remove the effects of joint Coulomb friction and of time-varying dynamic friction, a two nested multivariable loop control structure is proposed: we close an inner loop around the motor, that controls the joint (motor) angles; and then an outer loop is closed that controls the tip position. The general scheme of this control structure is shown in Figure 8. The inner controller uses the errors between the actual (Θ_m) and the commanded motor positions (Θ_{mr}), and generates control signals which are the currents for the two motors. The outer loop basically uses the errors between the actual (P) and the desired (P_r) positions, and generates control signals which are the command positions for the motors

at the inner loop. This scheme is the generalization to the multi-degree of freedom flexible arm case of a control scheme robust to friction developed in Feliu et al. [1-3].

As result of the procedure for controlling the motor position developed in the next subsection, we can describe the dynamics of the two closed-loop motors as two decoupled time invariant linear systems. And, if we use high enough gains in the controllers of these loops, the dynamics of these systems can be made much faster than the dynamics of the arm and, therefore, can be neglected in the design of the tip position control loop. This greatly simplifies the design method.

3.2. Motor position control loops

We use here the control scheme described in [1-3]. Let the dynamics of each motor be described by:

$$K_i \cdot i_i = J_i \cdot \frac{d^2\theta_{mi}}{dt^2} + V_i \cdot \frac{d\theta_{mi}}{dt} + CF_i + Ct_i, \tag{14}$$

where K_i is the electromechanical constant of the motor i, i_i is its current, J_i is its polar inertia, V_i is its dynamic friction coefficient, Ct_i is the coupling torque between this motor and the mechanical structure, CF_i is its Coulomb friction, and subindex $i = 1,2$, designates the motor.

Then we add to the current $\hat{i}_i$, generated by the motor position controller, two feedforward terms:

$$i_i = \hat{i}_i + (CF_i + Ct_i)/K_i, \tag{15}$$

the first one linearizes the motor system by compensating for the Coulomb friction which is nonlinear, the second one decouples the dynamics of the motor from the rest of the arm.

We assume that Coulomb friction is of the form:

$$CF_i(t) = \pm \mid CF_i \mid \tag{16}$$

where the sign is that of the motor velocity. Then the Coulomb friction compensation term is generated by knowing the amplitude of the Coulomb friction, and by estimating the actual velocity of the motor from position measurements. Comments to the velocity estimation procedure made in Subsection 4.1. of [2] remain valid.

In order to generate the decoupling term, the coupling torque Ct may be directly obtained from measurements of strain gauges placed at the joints, or can be estimated from the actual measurements of motor and tip positions following the procedure below:

1. Calculation of the equilibrium tip position $P_0 = \begin{pmatrix} \rho_0 & \gamma_0 \end{pmatrix}^T$ corresponding to the arm without any deflection, in the case in which the joint angles are the actually measured values θ_{m1} and θ_{m2}. P_0 is calculated from the direct kinematic model of the arm.

2. Calculation of the actual deflections, obtained from the actual tip position and P_0:

$$\delta = \begin{pmatrix} \rho - \rho_0 \\ \rho_0 \cdot (\gamma - \gamma_0) \end{pmatrix}.$$

3. Calculation of the external forces $F = \begin{pmatrix} F_\rho & F_\gamma \end{pmatrix}^T$, that applied to the tip generate such deflections. This is obtained from the stiffness matrix (inverting the compliance matrix).

4. Transformation of these tip forces into the corresponding reaction torques at the joints. These torques are the coupling torques Ct and can be obtained from expression (7).

This procedure gives an approximate estimation of the coupling torques because the expressions used here are only approximate. But experiments will show that these estimations are sufficient for decoupling purposes.

It was shown in [1],[2] that closing the motor position loop with high gain controllers makes the system more insensitive to perturbations (caused by an imperfect compensation of the Coulomb friction, a.e.), and to time varying parameters (dynamic friction coefficient, a.e.).

Figure 9 shows the resulting inner loop control scheme. The feedforward and feedback terms of the discrete feedback controllers (Kp_i and $B_i(z)$ respectively) are designed so that the response of this loop (motor-position-control) is significantly faster than the response of the outer loop (tip-position-control) and without any overshoot. This is done by making the gain of the feedforward controller large. It was shown in [1],[2] that, in theory, this gain could be made arbitrarily large even in the case of the arm being a non-minimum phase system. Practical limits to these gains are given by the saturation current of the D.C. motor amplifier, unmodelled high frequency dynamics, or even instability because of the discretization of the signals when using digital controllers.

It is important to mention that this controller is adequate only for steplike motor position references. It is used here because we expect that the commands for the motor will have approximately this shape (they will change very sharply). In other cases, a standard P.D. controller may be used.

When the closed-loop gain of the inner loop is sufficiently high, the motor position will track the reference position with small error. Then the dynamics of the inner loop may be approximated by 1 when designing the outer loop controller.

Then, summarizing, we want to achieve two objectives when designing a controller for the motor position:

1. to remove the modeling errors and the nonlinearities introduced by Coulomb friction and changes in the coefficient of the dynamic friction,

2. to make the position controlled response of the motor much faster than the response of the tip position control loop (outer loop in Figure 8).

And these objectives are accomplished by:

1. feedforward term that compensates for Coulomb friction,
2. feedforward term that compensates for coupling torque between arm and motors,
3. closing a high-gain feedback loop, that increases the robustness of the system and speeds the motor response.

The fulfillment of the second objective will allow us to substitute for the inner loop, an equivalent block whose transfer function is approximately equal to one; i.e. the error in motor position is small and quickly removed. This simplifies the design of the outer loop as will be seen in the next subsection.

3.3. Tip position control loops

We describe here the method used to control the tip position. In what follows we assume that the dynamics of the motor position loops (inner loops) are negligible compared to the dynamics of the arm. If this assumption holds, the arm dynamics may be cancelled using the scheme described in Figure 10 that transforms these dynamics into two decoupled double integrators. Then this method can be considered as an extension of the resolved acceleration method ([4], a.e.) to the case of lightweight two-link flexible arms. Once the system has been reduced, two independent P.D. controllers may be designed, one for each coordinate of the tip position. A feedforward term is added to avoid delays when following a trajectory, and some integral action is included in the controllers in order to remove small errors due to non exact modelling of the arm kinematics.

The dynamics-cancelling scheme has the following components:

1. First a positive feedback loop is closed, that uses the motor position calculated from the tip position assuming that there are not deflections in the arm (inverse rigid arm kinematics).
2. Inverse of the jacobian of the rigid arm kinematics. This component transforms the deflections expressed in terms of the tip position (difference in the tip position between the deflected and the undeflected arm for given motor angles), into deflections expressed in terms of motor position (difference in the motor position between the deflected and the undeflected arm for a given tip position).
3. Compliance matrix that relates the forces needed at the tip to move the mass as we want, with the deflections needed to achieve this.
4. Component that computes the inverse dynamics of the rigid arm (model (6)).

Notice that, in this procedure, we are cancelling block by block the arm dynamics expressed in Figure 7 (we exclude motor dynamics, that have already been cancelled by the inner loop). A scheme equivalent to this one was developed in [2], [3] for single-link lightweight flexible arms. Because we use a special configuration that decouples radial from angular motions, components 1 and 2 of that cancelling scheme are very simple: θ_{m1} may be approximately expressed as a linear function of φ and θ_{m2} as a linear function of ρ in component 1; and $\hat{J}$ is a constant diagonal matrix in component 2.

Finally, we mention that this scheme can be easily extended to lightweight flexible arms of n-degrees of freedom.

4. Experimental results

4.1. Apparatus

We have designed and built an apparatus to enable real-time control experiments with a two-joint, planar arm. As shown in Figure 11, the apparatus comprises an air table; arm, with tip mass, two actuators and joint sensors; camera for tracking position of tip-mounted, infrared LED; and control computer.

The mechanical system was designed to closely approximate the behavior of the ideal system; i.e. the arm is very light in weight, carries an effective point mass at its tip and has minimal friction and backlash. The arm is constructed of music wire, .047" and .063" diameter, and has a total mass of about .045 #m. The tip mass is a disk that floats on the air table, and has a pivoted connection so that it does not generate torques on the tip of the arm; thus it appears to the arm as a mass concentrated at the tip. Tip mass is adjustable by using different disks, but is typically 0.12 #m. Thus tip mass is substantially greater than arm mass, and a lumped-mass model is reasonable. Small ball bearings, used at the three passive joints of the arm, minimize friction. Tests have shown the friction on the air table to have negligible effect on the behavior of the system. The dimensions of the arm are: l = 9", $O - A$ = 3", and $B - C$ = 1.5". A strut was connected between the middle points of bars $A - B$ and $C - O$ in order to prevent buckling in link $A - B$; and to minimize the deviation from ideal behavior due to unequal bending in the two links (see Figure 12).

Joint actuators are DC torque motors. An Inland QT-2404B motor, rated at 36 #-in peak torque, drives the base link ($O - A$) directly. A second motor, Inland model QT-1207D, rated at 1.25 #-in, rides on the base link and generates torque between the base link ($O - A$) and first link ($O - C$), through a 3:1 gear reduction. Torques available from the motors are greater than the bending strength of the arm, so torque limits are not a factor in the tip-control servo. Motor response is generally fast compared to the tip response, although this is affected by amplifier current limits, which are adjusted in the range of .5 to 4 amps. One Inland model EM19-48030-B01 linear current amplifier is used for each motor. Experiments showed that Coulomb friction at the motor joints is considerable, so our method is especially appropiate to control this arm.

Three sensors are provided for control: one for each joint, and one for the tip. Joint sensors are single-turn potentiometers connected directly to the motor shafts: a 2" unit for the larger motor (QT-2404) and a 7/8" unit for the smaller. A Hamamatsu tracking camera, model PSD, with infrared passing filter, provides ±5v signals for the x and y positions of an LED attached to the tip. Range of travel within the field of view of the camera is between 7-15" in x axis and about ±4" in y axis.

A Sun/Ironics computer system provides for real-time control, program development, and data display and analysis. The system includes a Sun 3/160 workstation and Ironics IV3201 CPU connected via the Sun VME bus, and Ironics IV1645-01 A/D and IV1640-01 D/A boards providing analog input and output. The Sun provides a networked Unix environment for program development, interface with the the real-time control hardware, and storage and display of data. Control programs are written in C, and compiled to run on the Ironics CPU, under the Chimera operating system developed at CMU for real-time control. Chimera provides process scheduling and control primitives that facilitate real-time control programming, while emulating many UNIX utilities for programming convenience.

4.2. Identification

The dynamics of the arm have been divided, for modelling and control purposes, into two submodels: motors submodel and mechanical structure submodel, which are coupled by the torques at the two motors (see Figure 13). It was shown that this way of modelling flexible arms has some advantages over other methods when dealing with arms with strong Coulomb friction in the joints [1-3]. In our identification procedure, we follow this approach identifying both submodels separately.

4.2.1. Mechanical Structure

We use here the experimental method indicated in Subsection 2.3.. We immobilized the two motors, we deflected the arm by applying an arbitrary force to the tip, and then released the tip. The oscillation produced at the tip had two orthogonal components of different frequencies, as it was stated in Section 2.

In order to know the two vibrational modes and their directions, we used the following technique:

1. Record the $x - y$ motion of the tip.
2. Calculate the Fourier transform of these two signals $x(t)$ and $y(t)$.
3. The spectral analysis shows that $x(\omega)$ presents two peaks x_1 and x_2 at frequencies ω_1 and ω_2; and $y(\omega)$ has other two peaks y_1 and y_2 at the same frequecies ω_1 and ω_2 as $x(\omega)$. ω_1 and ω_2 are the frequencies of the two vibrational modes. And the directions of the axes of oscillation are calculated from the expression:

$$\psi_i = \arctan(\frac{y_i}{x_i}) \quad i = 1,2. \tag{17}$$

This procedure is repeated for different arm configurations (different ρ). We used the $Matrix_x$ package for analysis and simulation of control systems. In particular, we calculated the above mentioned Fourier transforms using the FFT routine of this package. Experimental results are given in the next table for our particular arm:

ρ (inches)	$\rho/(2 \cdot l)$	ω_1 (hz)	ψ_1 (degrees)	ω_2 (hz)	ψ_2 (degrees)	k_b $(in \cdot \#)$	k_c $(in \cdot \#)$
10.1	0.56	0.6514	13.7781	2.1983	106.1437	11.57	6.14
10.55	0.59	0.6839	14.3237	2.1332	102.3821	12.3	6.54
11.0	0.61	0.6839	15.3966	2.0844	104.9338	11.6	6.58
11.6	0.64	0.7328	17.2057	1.9866	103.7644	12.9	6.77
12.2	0.68	0.7491	19.0925	1.9215	104.1487	12.5	6.82
12.6	0.7	0.7653	20.9127	1.9052	111.4644	12.5	6.87
13.0	0.72	0.7816	22.6677	1.90	112.6137	12.3	6.99
13.6	0.76	0.7979	26.173	1.9215	116.3932	11.9	7.0
14.0	0.78	0.7979	28.5903	1.8889	119.2472	11.3	6.75

Table. Experimental vibrational modes.

where the stiffnesses of the single links k_b and k_c are calculated using the following procedure:

1. Calculate the compliances c_u and c_v in the principal coordinate axes using the expression

$$c_u = \frac{1}{m \cdot \omega_1^2}, \qquad c_v = \frac{1}{m \cdot \omega_2^2}.$$

2. Calculate matrix C, from c_u and c_v, by carrying out the matrix transformation that corresponds to rotating an angle ψ_1 these main axes.

3. Calculate k_b and k_c from expressions (10)-(12).

These experimental results show that values k_b and k_c are quite consistent. We will use in our control the average of the table values: k_b = 12.1 and k_c = 6.7. Notice that both modes are approximately orthogonals: $\psi_2 = \psi_1 + 90$.

Finally, in order to complete the verification of our theoretical model, we took out the strut between bars $A - B$ and $C - O$ (to simplify the model and the verification), and repeated the experiment for one configuration:

ρ (inches)	$\rho/(2 \cdot l)$	ω_1 (hz)	ψ_1 (degrees)	ω_2 (hz)	ψ_2 (degrees)	k_b $(in \cdot \#)$	k_c $(in \cdot \#)$
10.55	0.59	0.6188	11.5842	2.003	100.6535	9.09	6.39

The theoretical individual stiffnesses were calculated for this case, using our massless flexible arm model, and they were: 9.02 $in \cdot \#$. and 6.63 $in \cdot \#$., which substantially agreed with the result of this last experiment. All these results confirm the assumption of arm with massless links and joints, with all its mass concentrated at the tip.

4.2.2. Motors Parameters

In order to identify the motor submodel, the mechanical structure (links) was taken out from the motors. Then the coupling torque between motors and arm was zero (Ct_i in expression (14)), and the motors could run freely. In what follows, the parameters of the second motor, which has some reduction, will not be given in motor terms but in joint terms.

First, we identified the Coulomb friction CF_i because it is a nonlinear term. We obtained Coulomb friction values from measuring the current at which the motors started to move and they were: 0.12 *amps.* for the first motor and 0.16 *amps.* for the second. Once we knew them, we were able to approximately compensate for the Coulomb friction by adding a term to the current with the estimated absolute value and the sign of the motor velocity, as was described in Subsection 3.2.

After compensating for the Coulomb friction, the remaining dynamics are linear and can be identified by any of the standard techniques. The model is now:

$$\frac{\theta_{mi}(s)}{\hat{i}_i(s)} = \frac{\frac{K_i}{J_i}}{s \cdot (s + \frac{V_i}{J_i})}, \qquad i = 1, 2. \tag{18}$$

The parameters that remain to be identified are the motor inertias J_i and the dynamic frictions V_i. The electromechanical constant of the motors K_i are obtained from catalog. We estimate J_i and V_i from the

frequency response of the system. The Bode plot of the magnitude of the frequency response shows that the response has a slope of -20 db at low frequencies and -40 db at high frequencies. These parameters can be easily calculated from two points of this plot. We used the following two points: the point at which the slope changes from -20 to -40 db, and a point at high frequencies. The identified transfer functions were:

Motor 1 :

$$\frac{\theta_{m1}}{\hat{i}_1} = \frac{636.5}{s \cdot (s + 16.38)} \tag{19}$$

Motor 2 :

$$\frac{\theta_{m2}}{\hat{i}_2} = \frac{23150}{s \cdot (s + 35.3)}. \tag{20}$$

4.3. Control

4.3.1. Motor control loop

The decoupling term of Figure 9 was implemented, as well as the compensation term for the Coulomb friction. Controllers for the motor position were designed according to this scheme. We tried to make the response of the motors as fast as possible, but without having any overshoot. Limits in the velocity of response were given by the amplifier current limits, which were 4 *amps.* for the first motor and 2 *amps.* for the second. We used a sampling time of 3 *msec.* in this inner loop.

The following experiment was carried out to test the motor control: the tip was kept fixed in the position (12 *inch.*, 0 *mrad.*) in polar coordinates, and steplike position commands were generated for the motors. The commanded positions for the motors were such that would have placed the tip in positions (10.82 *inch.*, -50 *mrad.*) and (13.18 *inch.*, 50 *mrad.*) if the tip had been free. Because the tip was fixed at the intermediate position between these two, the arm experienced substantial bending when the motors tried to follow these trajectories, and the coupling torques Ct_i were significant. Figure 14 shows the motor responses and the currents obtained in this experiment using the control scheme of Figure 9. The responses have nearly zero steady-state error which shows the effectiveness of the coupling torque and Coulomb friction compensation. The settling time is about 80 *msec* in both motors; this means that the time constants of the motor control loops are about 20 *msec.* These dynamics are significantly faster than the dynamics of the mechanical structure (modes of vibration), confirming the assumption that the inner loop dynamics are negligible. Figure 15 shows the responses when the coupling torque compensation term has been removed, and Figure 16 shows the responses when the Coulomb friction compensation term has been removed. The basic effects of removing these terms are the permanent errors that appear in these last two figures, the transient responses experience little change.

4.3.2. Tip control loop

The scheme of Figure 10 is used here to control the tip position. The motions are directly commanded in polar coordinates, so the first block of that figure, that transforms from cartesian to polar coordinates, is not needed. Second order parabolic profiles are used as reference trajectories, so the reference ρ_r describes a parabola and so does γ_r. The sampling time of the tip position control loop is also 3 *msec.*, like in the motor loop.

P.D. controllers were used first, instead of P.D.I.'s. We wanted the same response in ρ and γ, so the two P.D. controllers had about the same coefficients. Measurements given by the camera had significant noise so the estimations of the velocities, needed in the derivative term of the P.D. controllers, were obtained by using the discrete differentiation $(1 - z^{-5})/(5 \cdot T)$ instead of the typical $(1 - z^{-1})/T$. Experimental results showed good agreement with the theoretical analysis of the temporal response, but they showed a permanent error probably caused by kinematic modelling errors. Then, in order to remove that error, we used P.D.I. controllers for both ρ and γ loops.

We carried out experiments on arm tip positioning using the complete scheme of Figure 10. We moved the arm from the point (10.82 *inch.*, -100 *mrad.*) to the point (13.18 *inch.*, 100 *mrad.*) and viceversa. We programmed a high speed motion (it had to go from one position to the other in 0.4 *sec.*). Responses are shown in Figures 17 to 26. Figure 19 shows the estimated tip velocity in polar coordinates; and Figure 20 shows that motors follow very closely their references, confirming the assumption that the dynamics of the inner loop are negligible. This motion was then repeated under limit conditions, using the maximum allowable accelerations (now the motion was programmed to last 0.2 *sec.*). The results are shown in Figures 27 and 28.

5. Conclusions

Lightweight arms have the advantages of being easy to move, and being more efficient than heavier arms because very little energy is wasted in moving the arm structure. In turn, these arms usually exhibit some flexibility phenomena that cause nearly undamped oscillations to appear in the mechanical structure during the motion.

A two-degree-of-freedom, planar, very lightweight flexible arm has been designed, built and controlled in our laboratory. The motor of the second joint was mounted near the base of the arm to minimize inertia, and a four-bar linkage transmitted the motion from the motor to this joint. This linkage was specially designed to approximately decouple radial from angular tip motions. This arm exhibited two orthogonal vibrational modes that changed in value and orientation with the configuration.

A simple dynamic model has been developed for this arm based on the use of two submodels: one to describe the motors, and the other to describe the mechanical structure, the two coupled through the torques that the links generate on the motors. A control scheme has been deduced from this model which is robust to changes in the dynamic friction of the motor, and that removes the effects of the Coulomb friction. This control scheme is based on very simple concepts, and each term of the controller is designed according to very precise directions: terms that cancel Coulomb friction, terms that decouple the motors from the arm, inner loop controller to make the motor response fast, cancelling terms for the mechanical structure dynamics, feedforward term for the tip response, etc.

Experimental results have been presented, and they show that our control scheme performs well.

Our control scheme is based on the assumption that motor dynamics are much faster than mechanical structure dynamics. This point must be confirmed before closing the tip position loop. The decoupling between radial and angular motions achieved by the four-bar linkage simplifies kinematic considerations, but is not a necessary condition of our control method.

Finally, this method may be easily extended to lightweight flexible arms with any number of degrees of freedom.

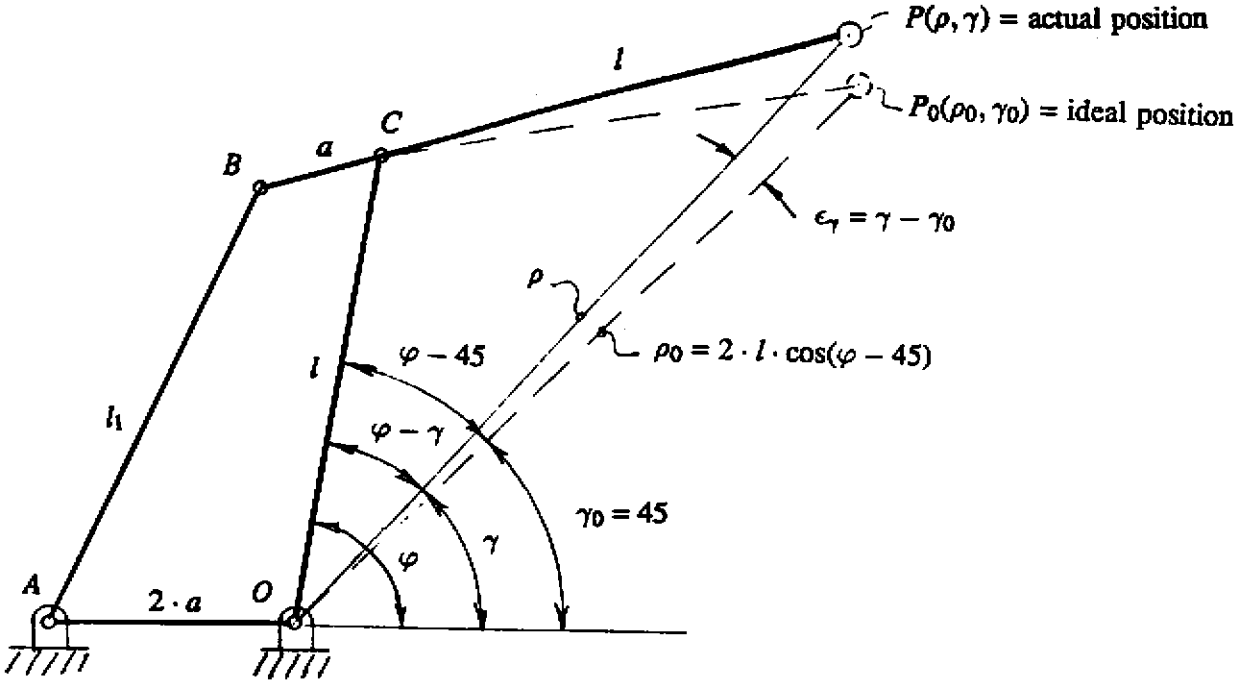

Figure 1: Arm geometry.

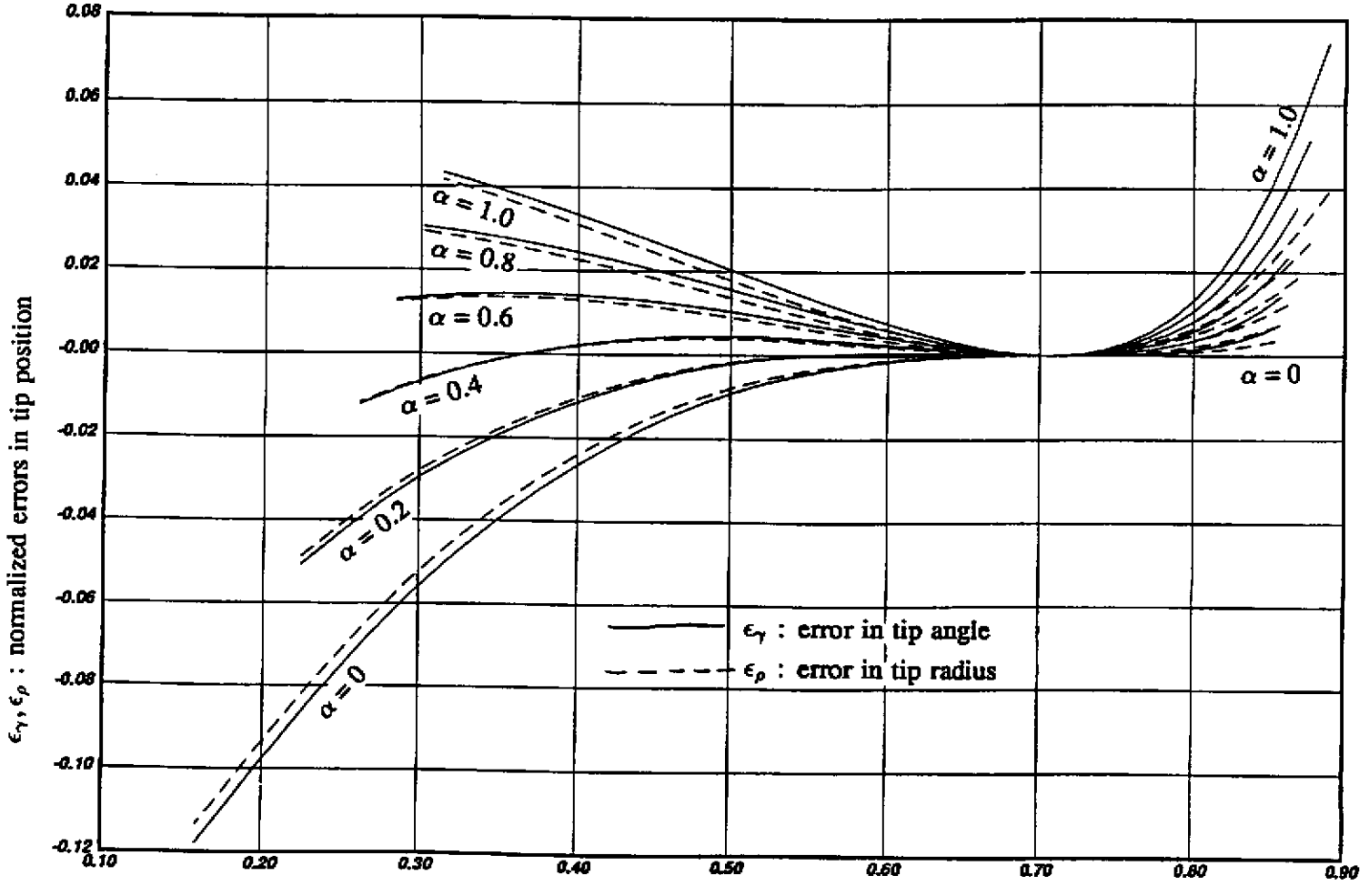

Figure 2: Kinematic errors.

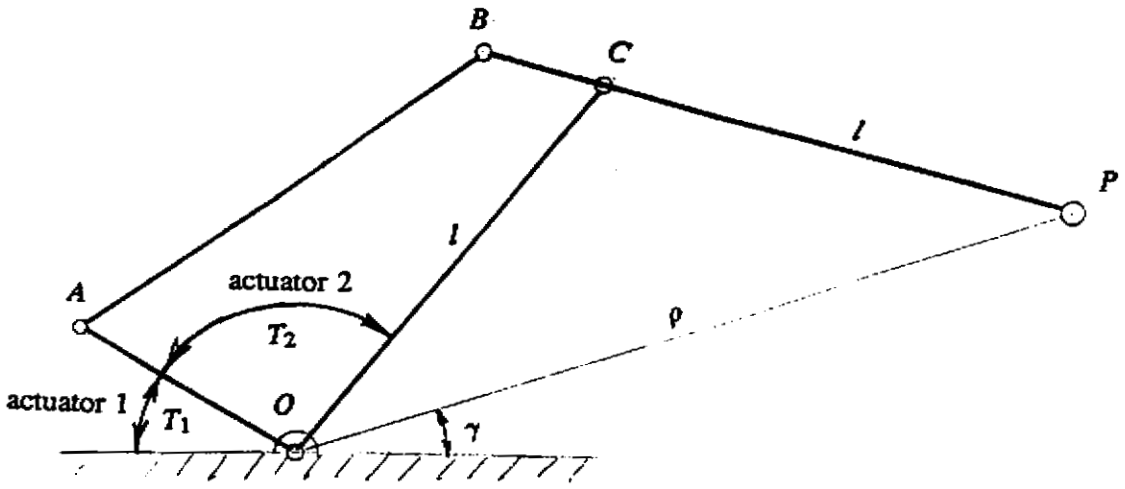

Figure 3: Actuators location.

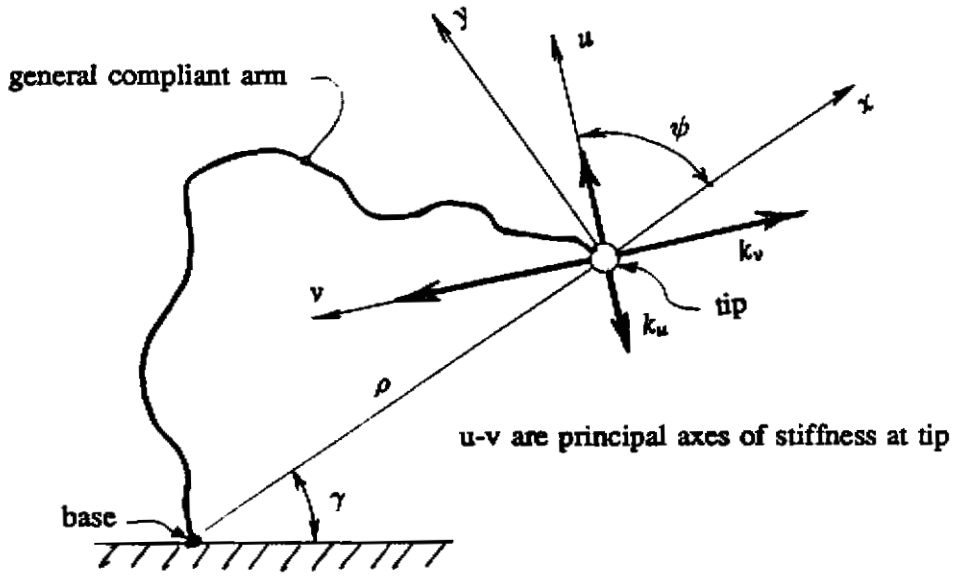

Figure 4: Two degrees of freedom compliant arm.

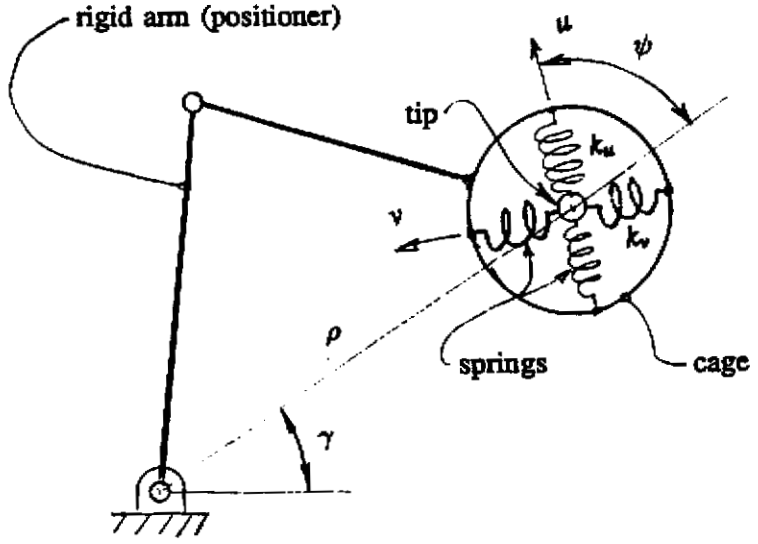

Figure 5: Equivalent spring model of lightweight two d.o.f. flexible arms.

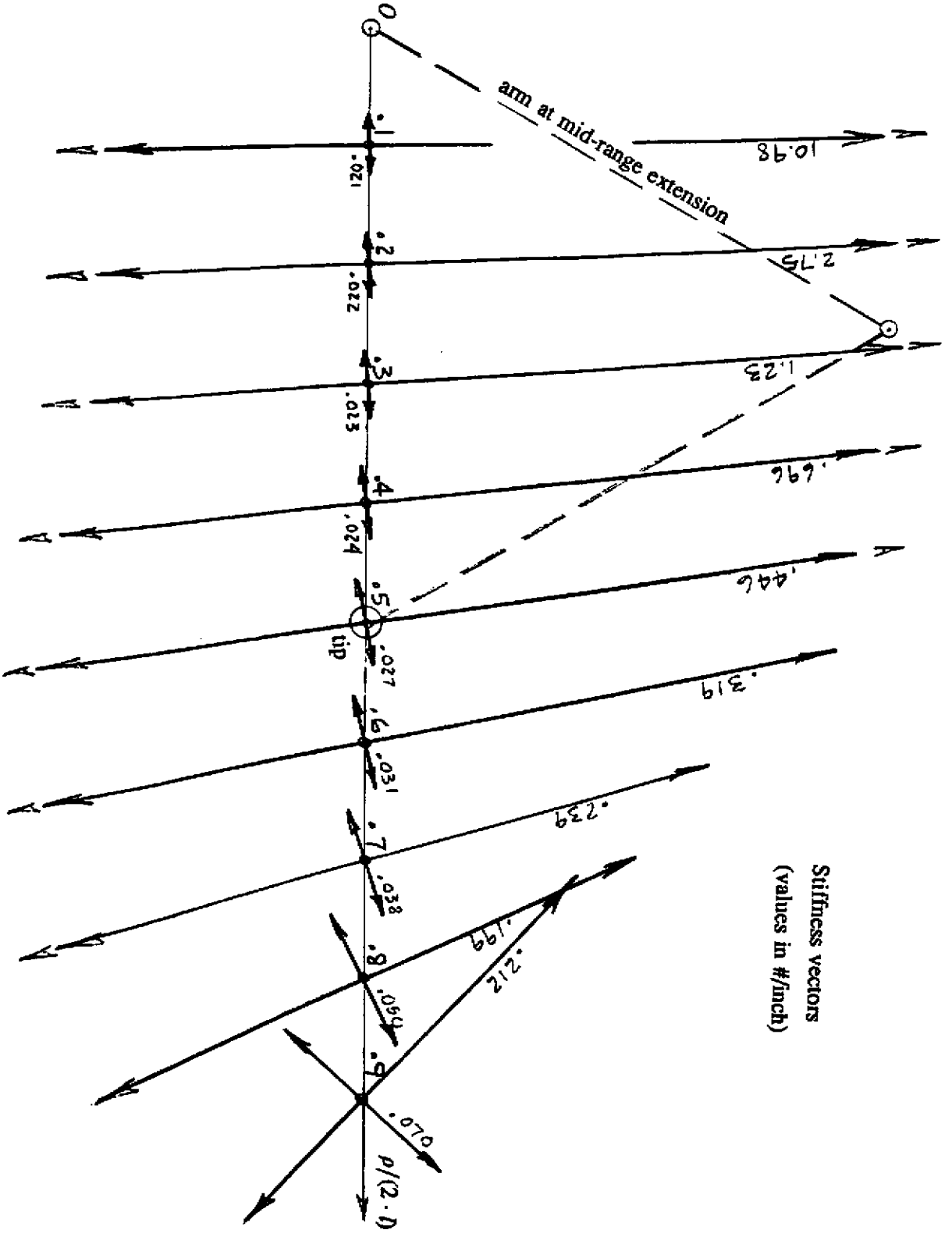

Figure 6: Stiffness plot.

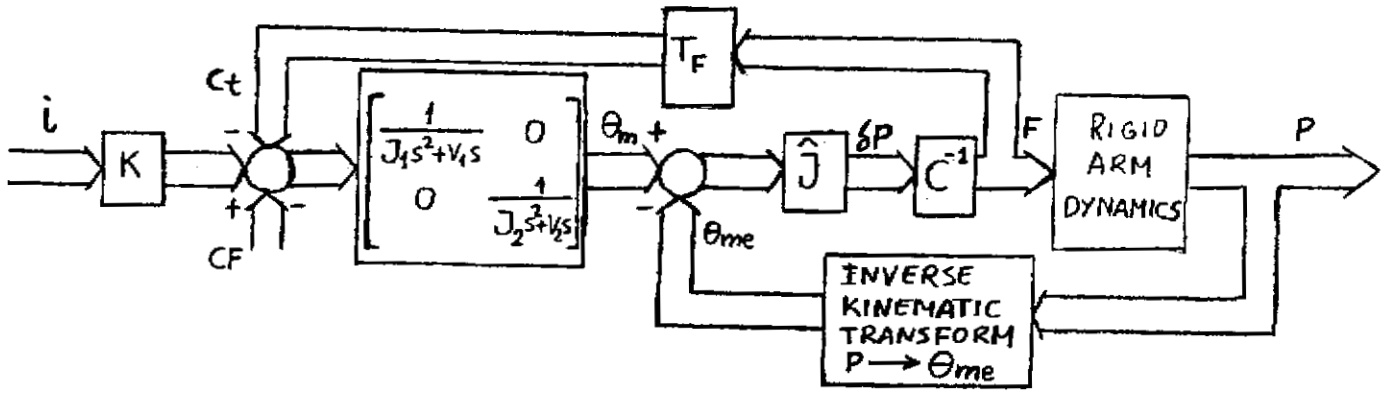

Figure 7: Dynamic model of a lightweight flexible arm.

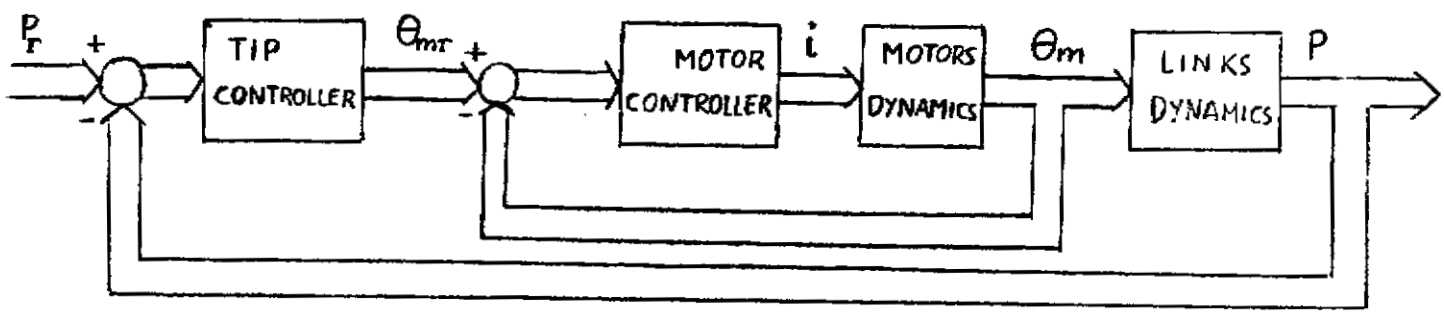

Figure 8: Control scheme insensitive to friction.

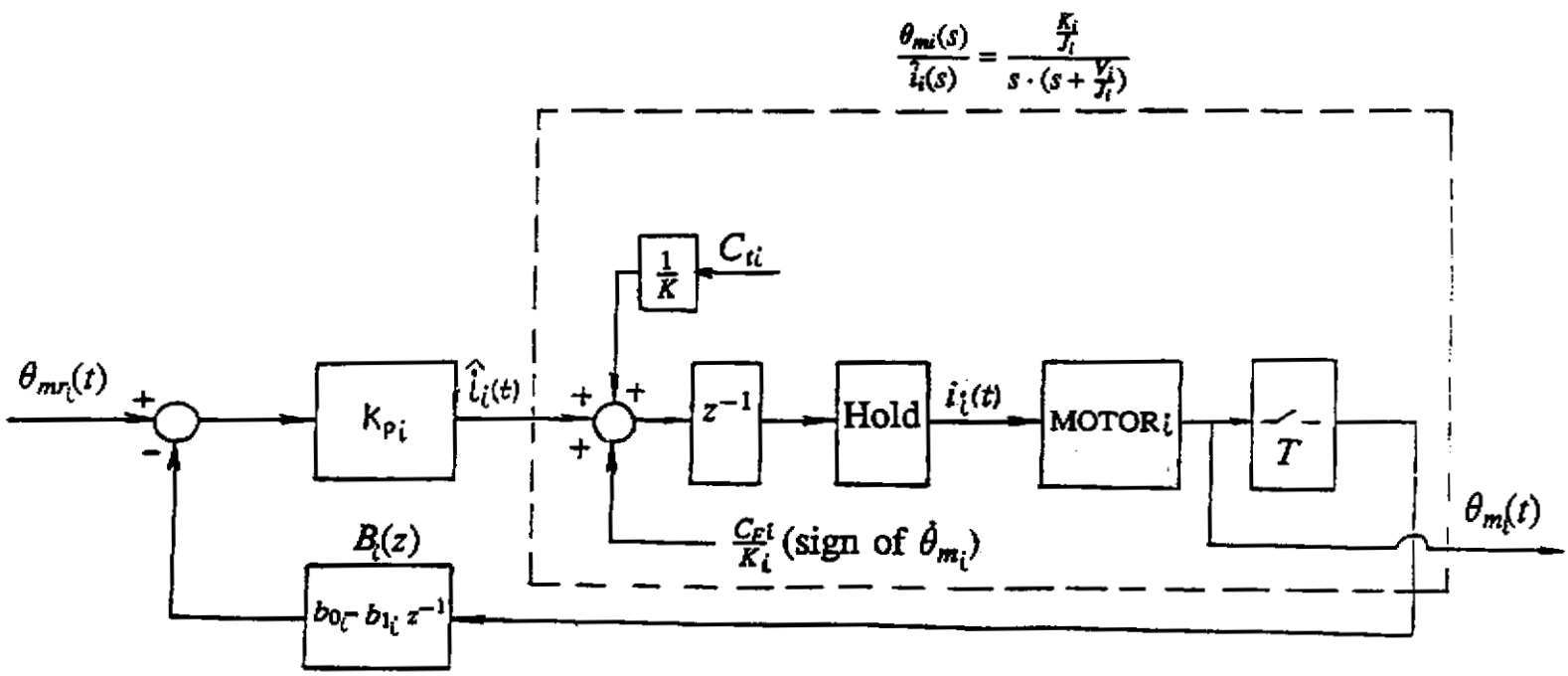

Figure 9: Implementation of the inner loop in one motor.

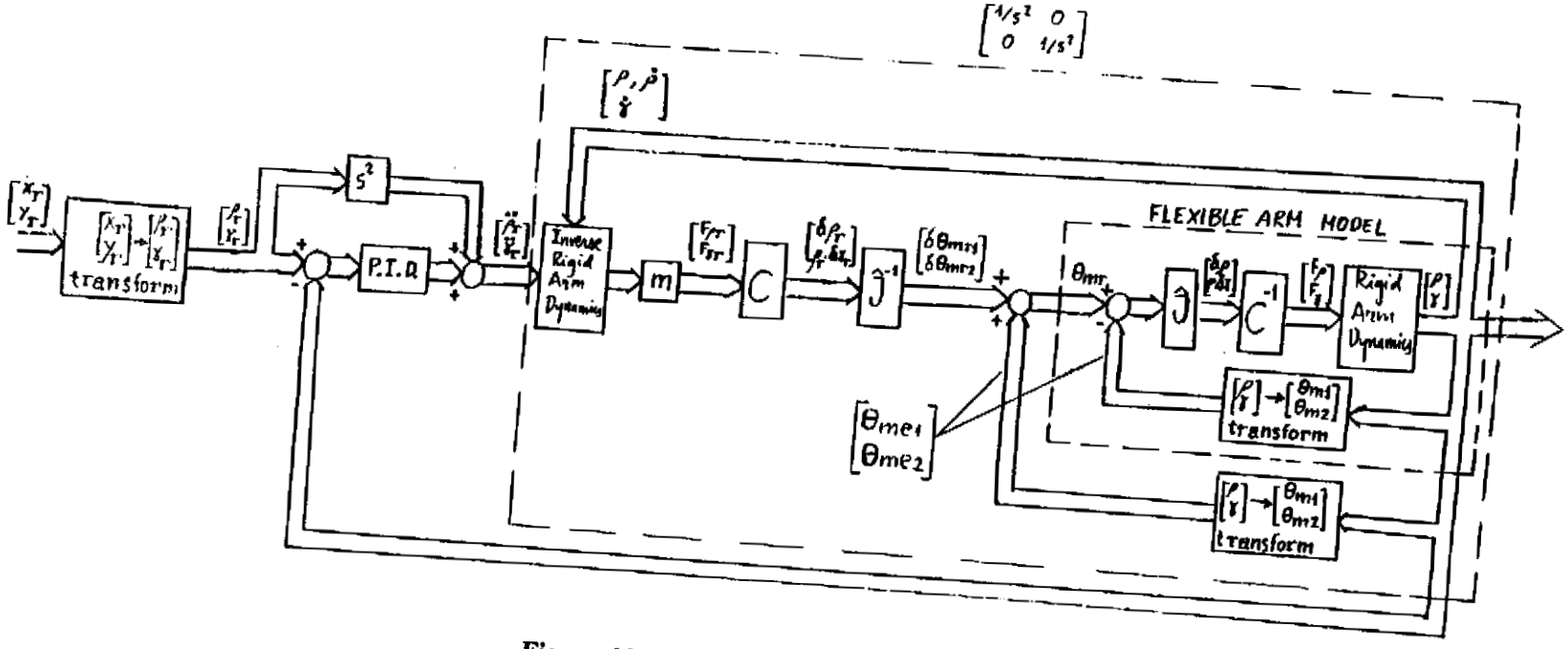

Figure 10: Tip position control scheme.

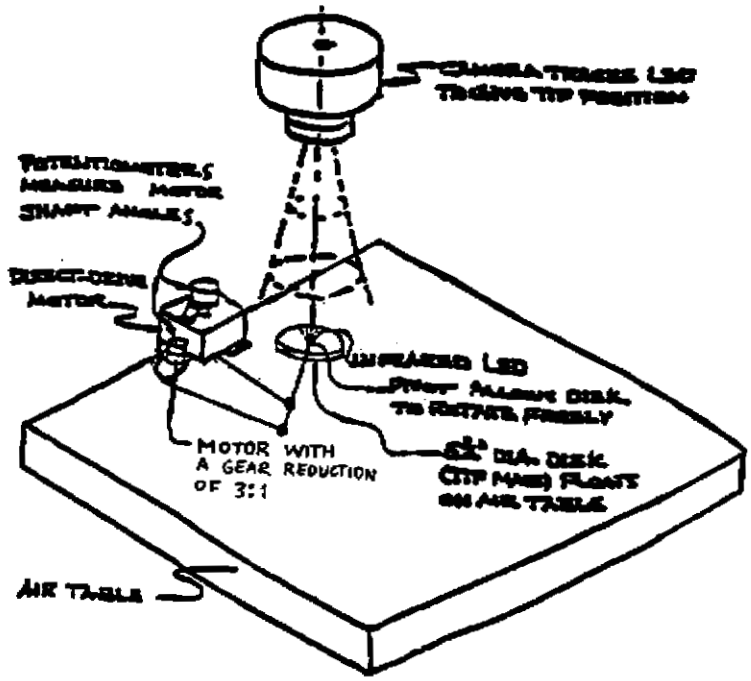

Figure 11: Experimental setup.

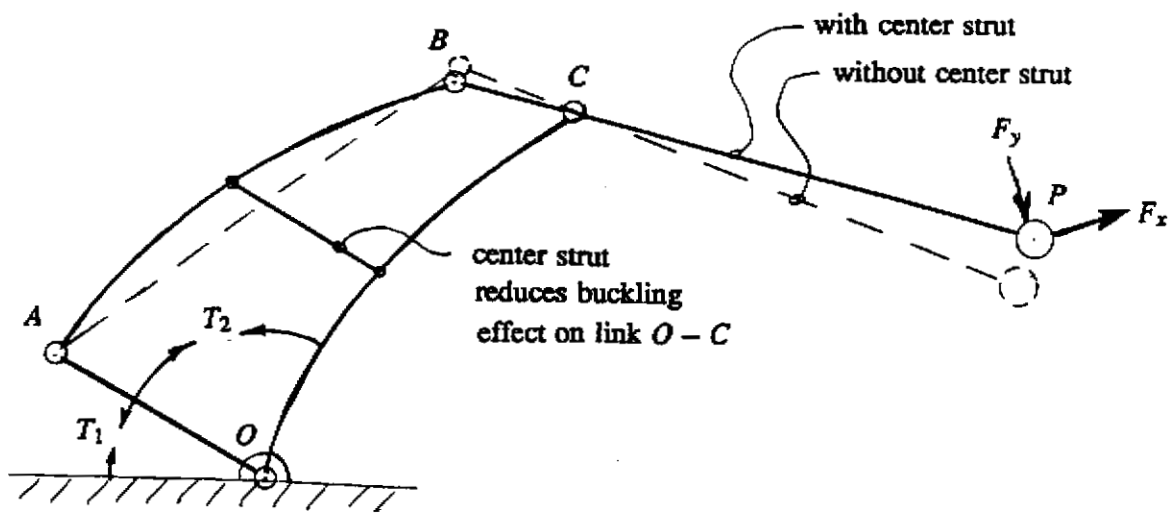

Figure 12: Buckling problem.

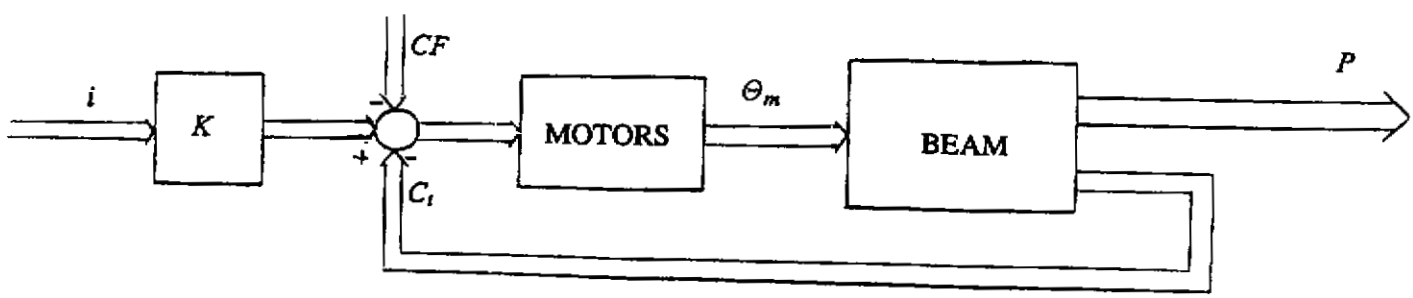

Figure 13: Flexible arm submodels.

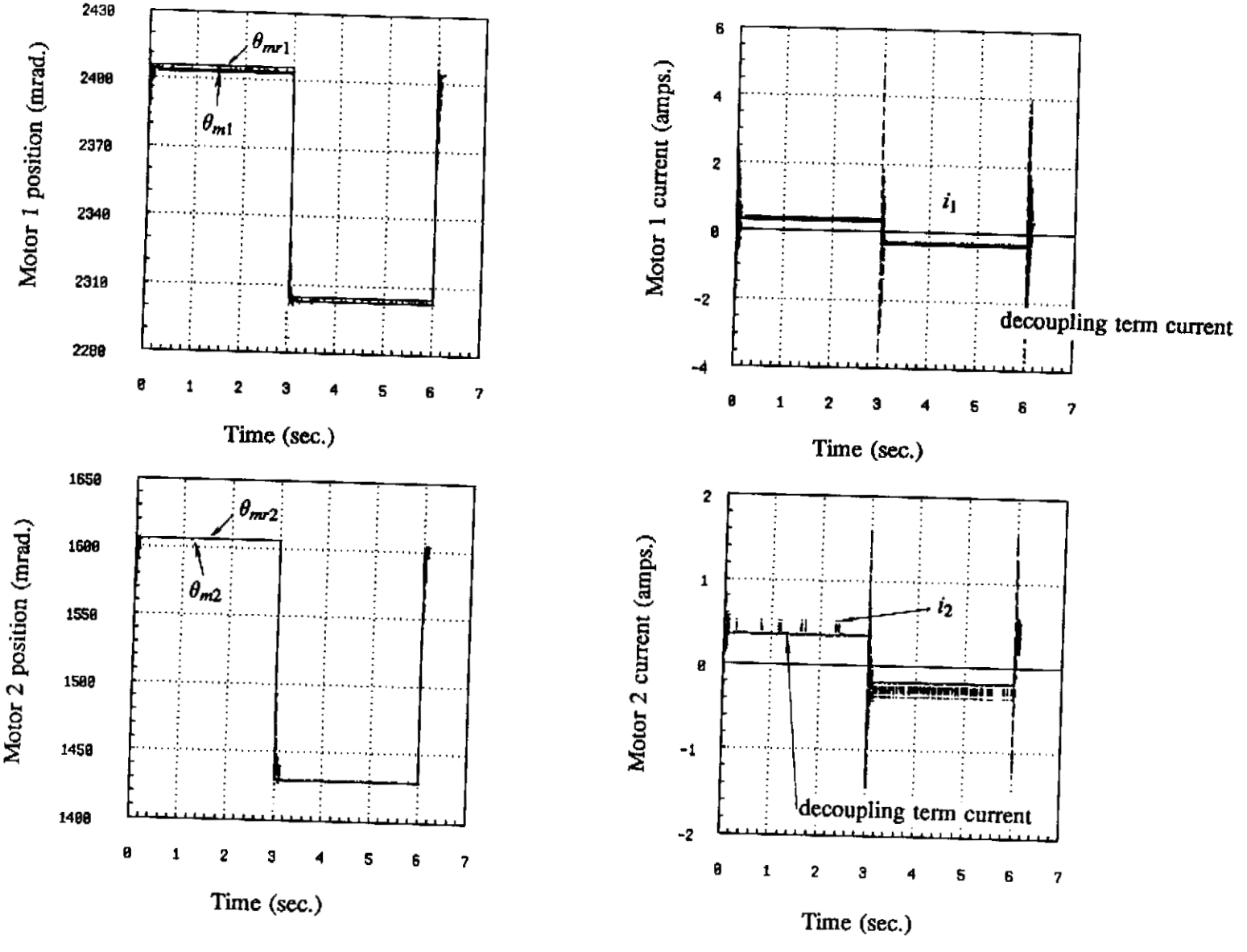

Figure 14: Responses of the inner loop with the complete controller.

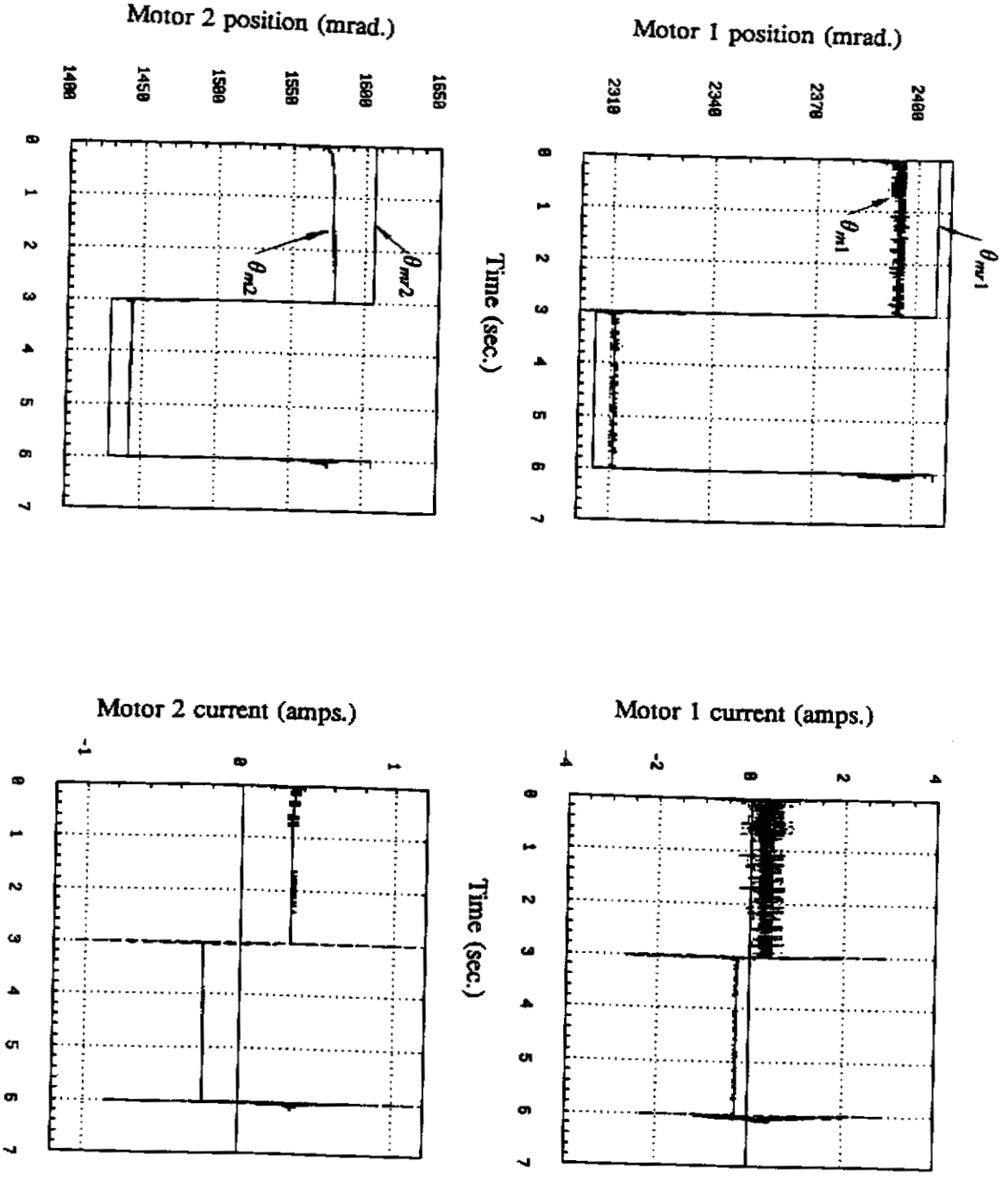

Figure 15: Responses of the inner loop without the decoupling term.

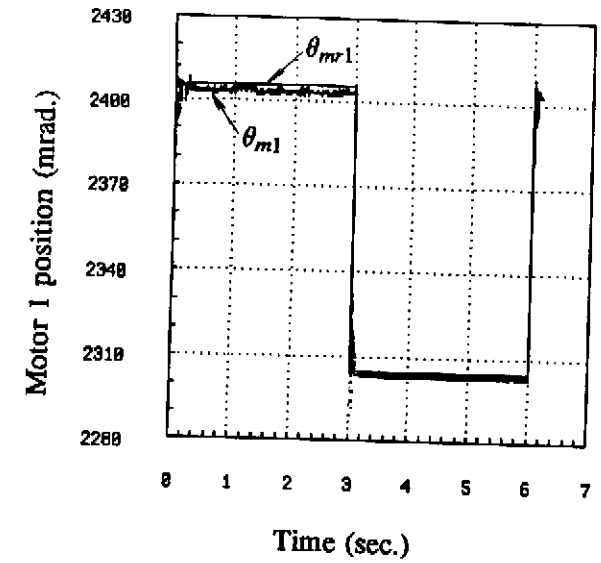

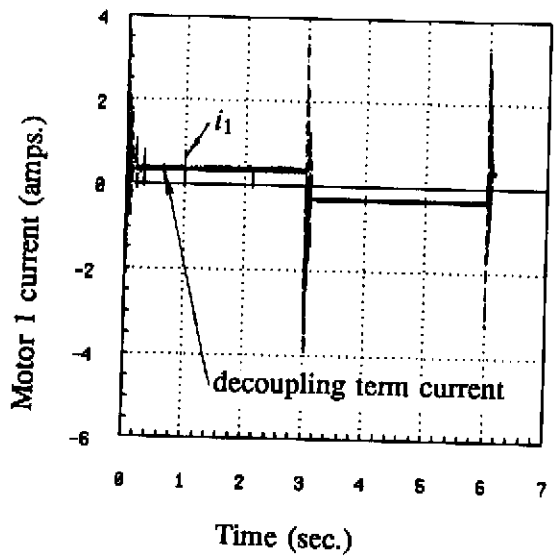

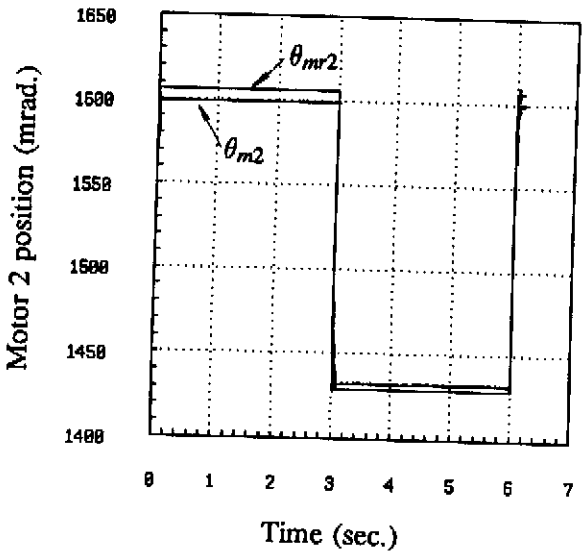

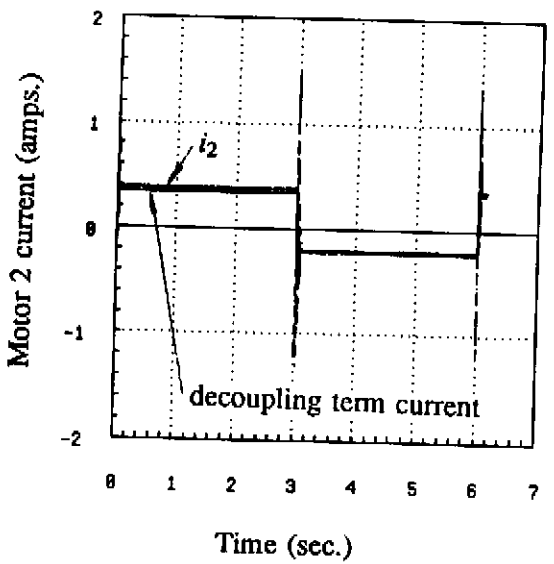

Figure 16: Responses of the inner loop without the Coulomb friction compensation term.

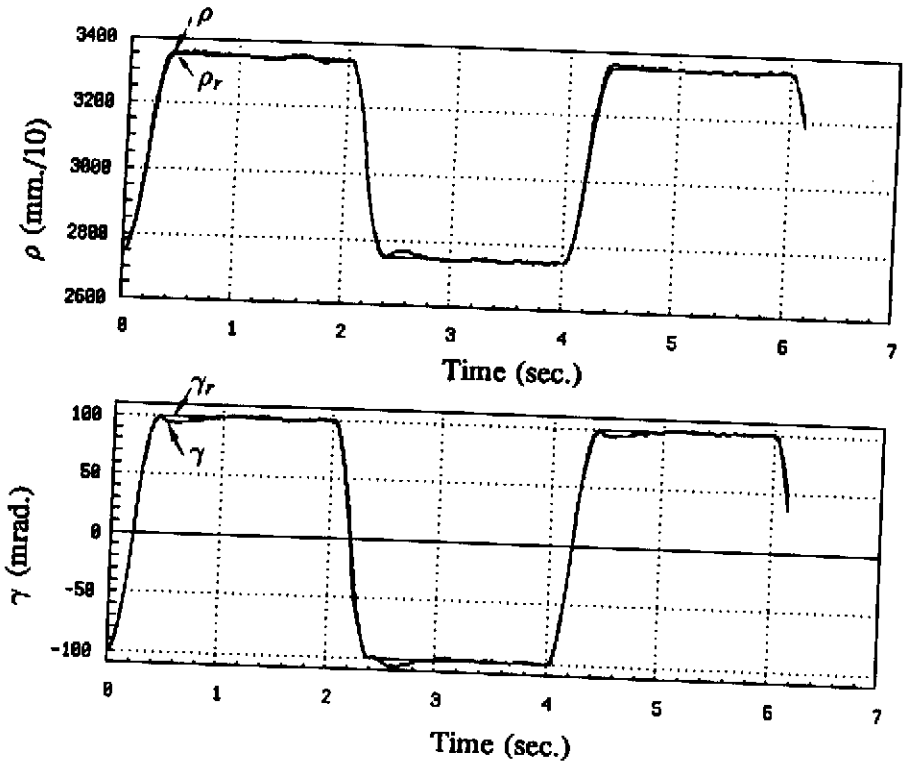

Figure 17: Tip response in polar coordinates.

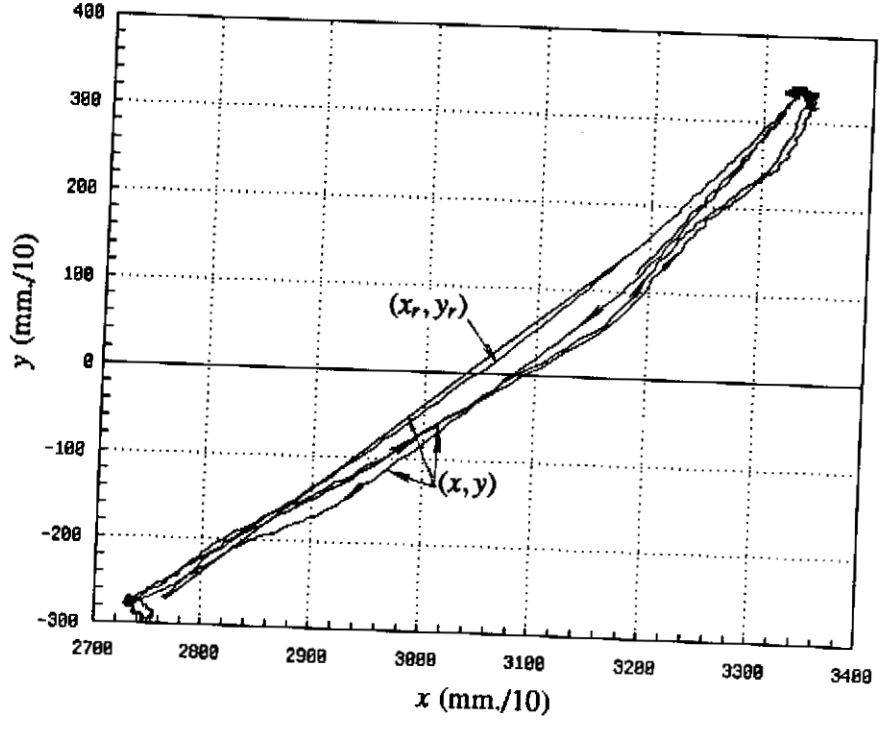

Figure 18: Tip response in cartesian coordinates.

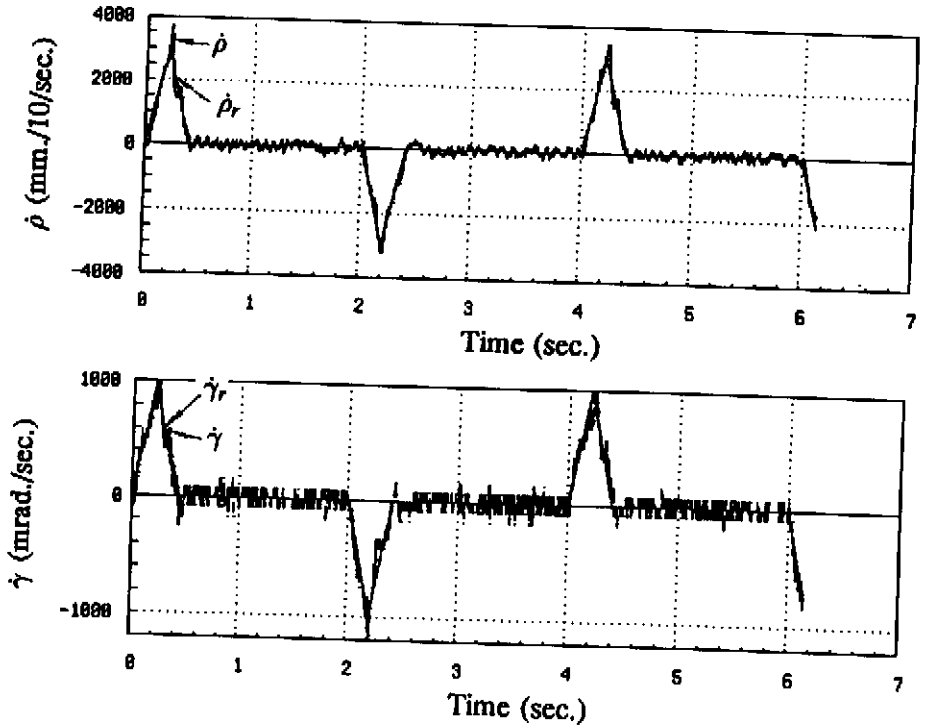

Figure 19: Tip velocities in polar coordinates.

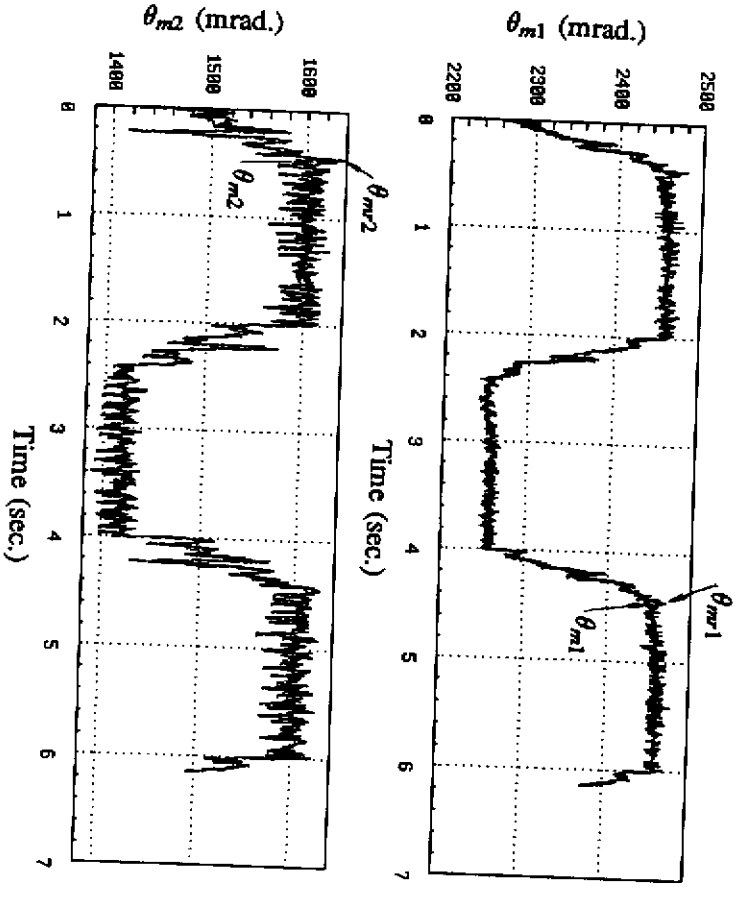

Figure 20: Motors responses.

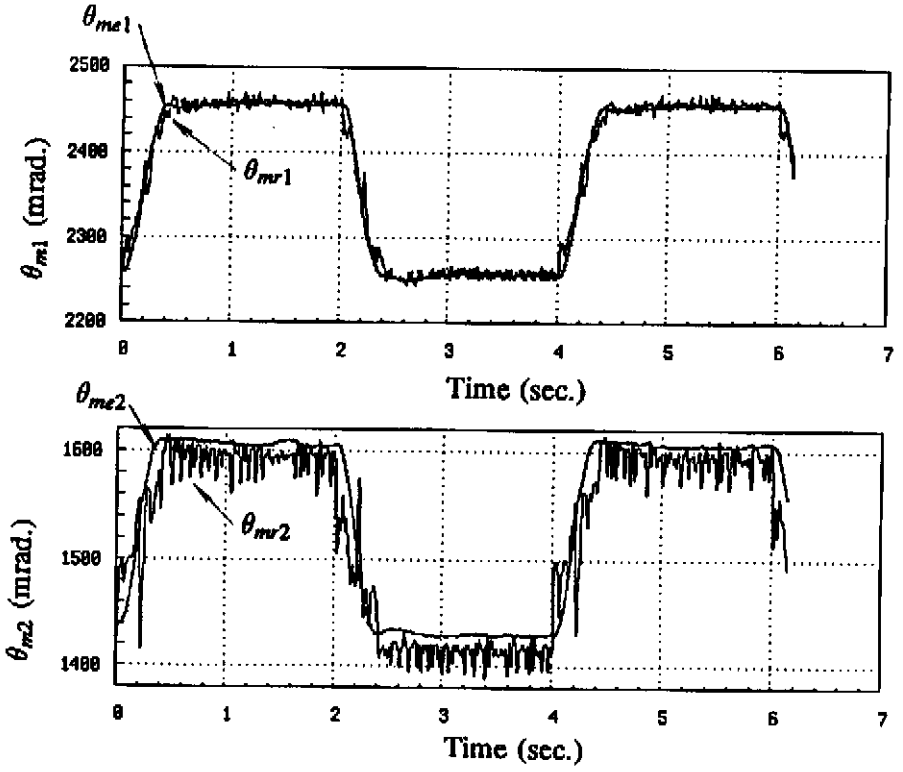

Figure 21: Comparison between the reference motor positions and the motor positions obtained from tip measurements assuming a rigid arm.

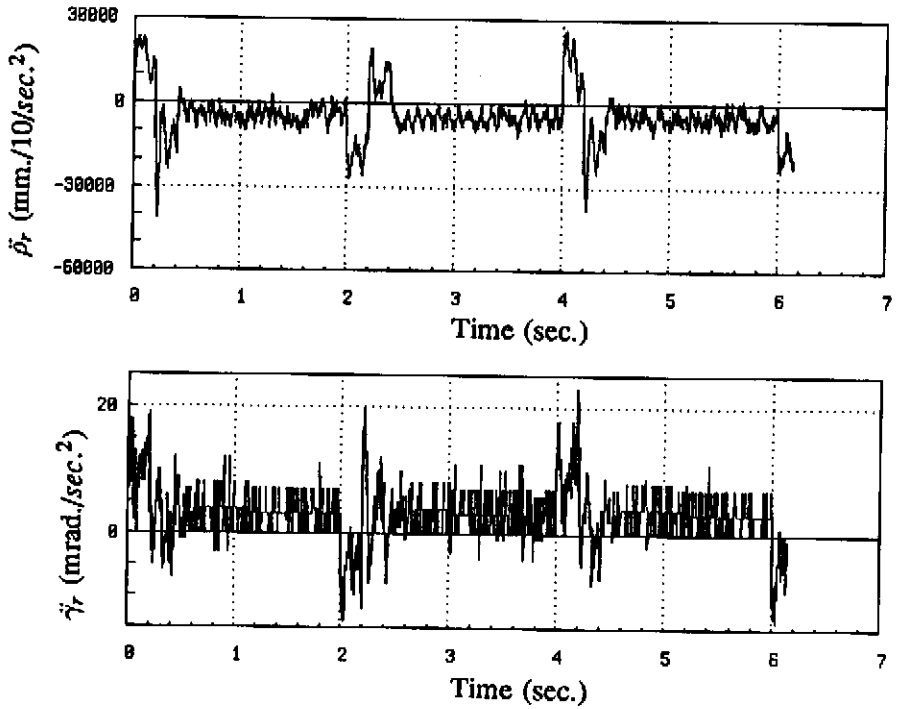

Figure 22: Reference tip acceleration (in polar coordinates).

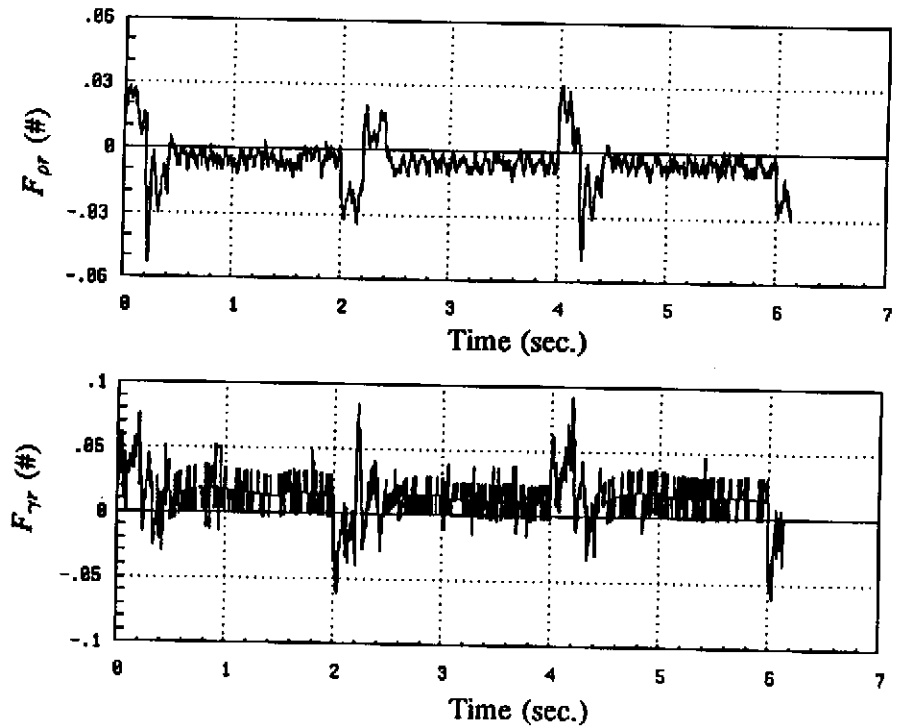

Figure 23: Forces that we want to apply to the tip to achieve the desired acceleration (in polar coordinates).

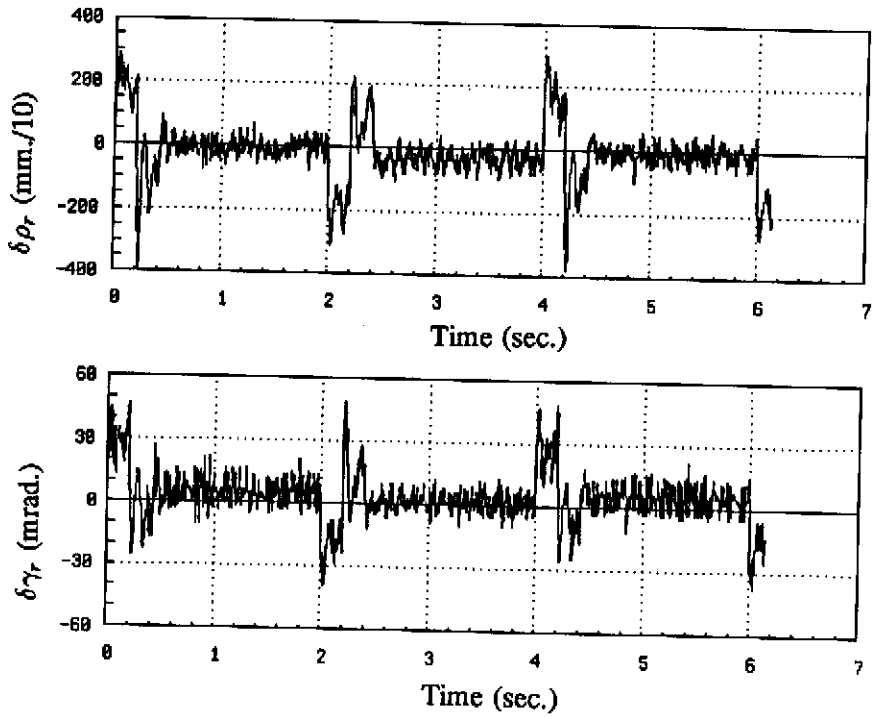

Figure 24: Deflections required to obtain the desired forces at the tip (in polar coordinates).

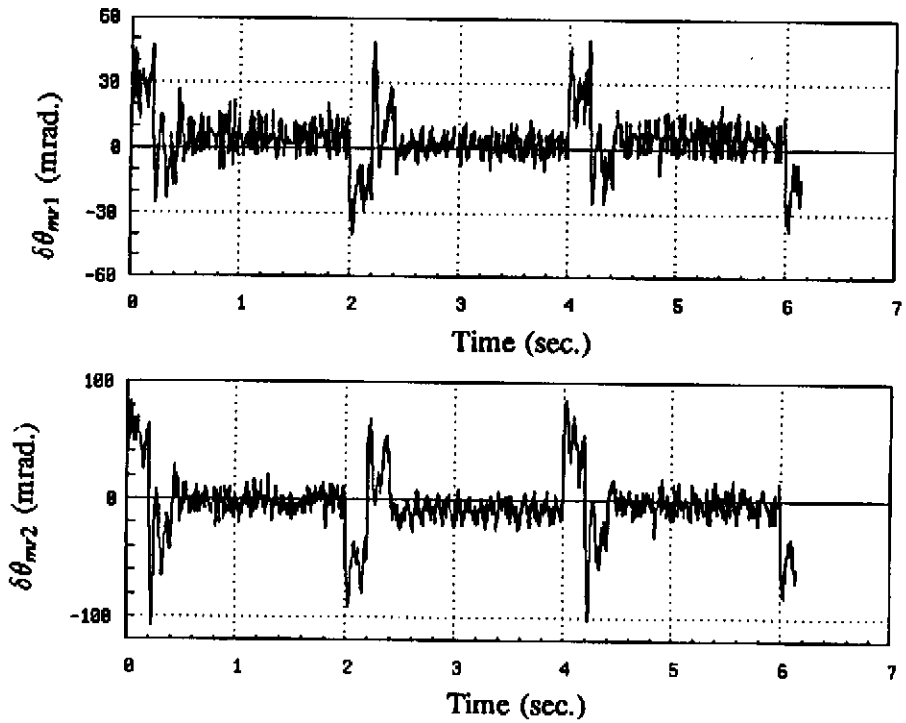

Figure 25: Increments needed in the motor positions (over the undeflected positions corresponding to actual tip coordinates) in order to produce the desired deflections.

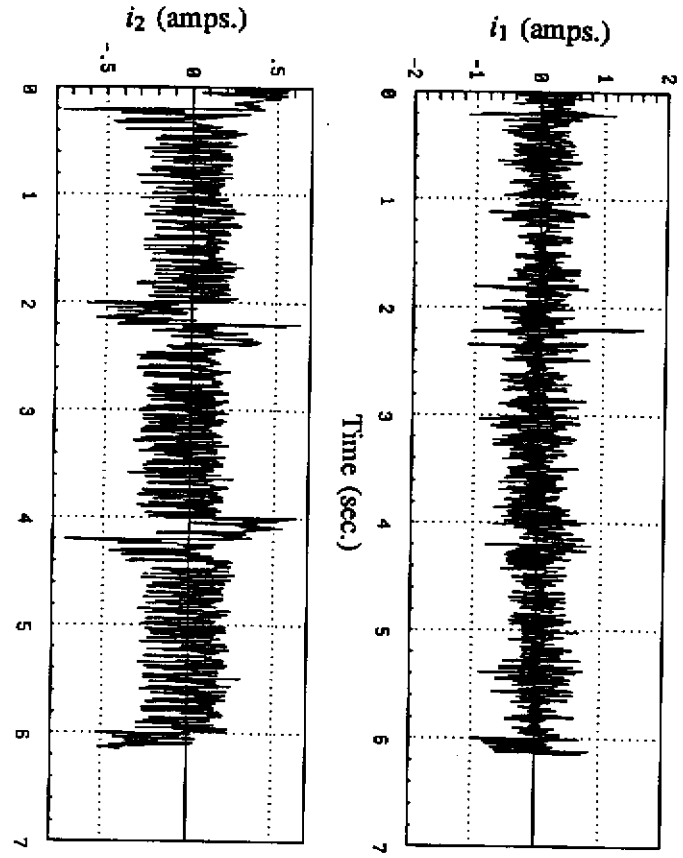

Figure 26: Currents applied to the motors.

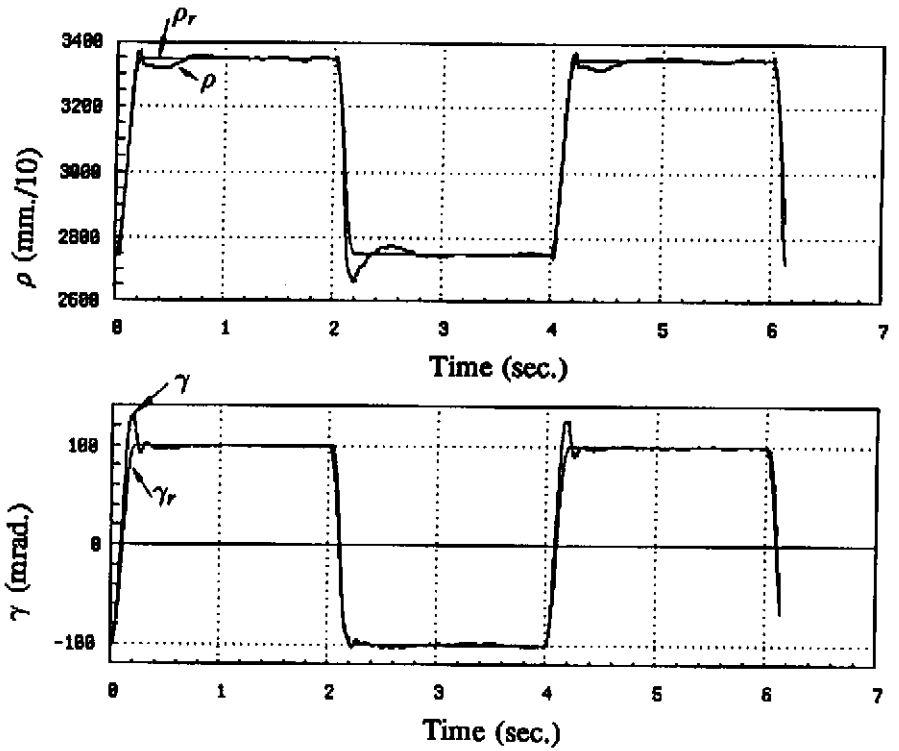

Figure 27: Tip response in polar coordinates to a trajectory with the maximum allowable accelerations.

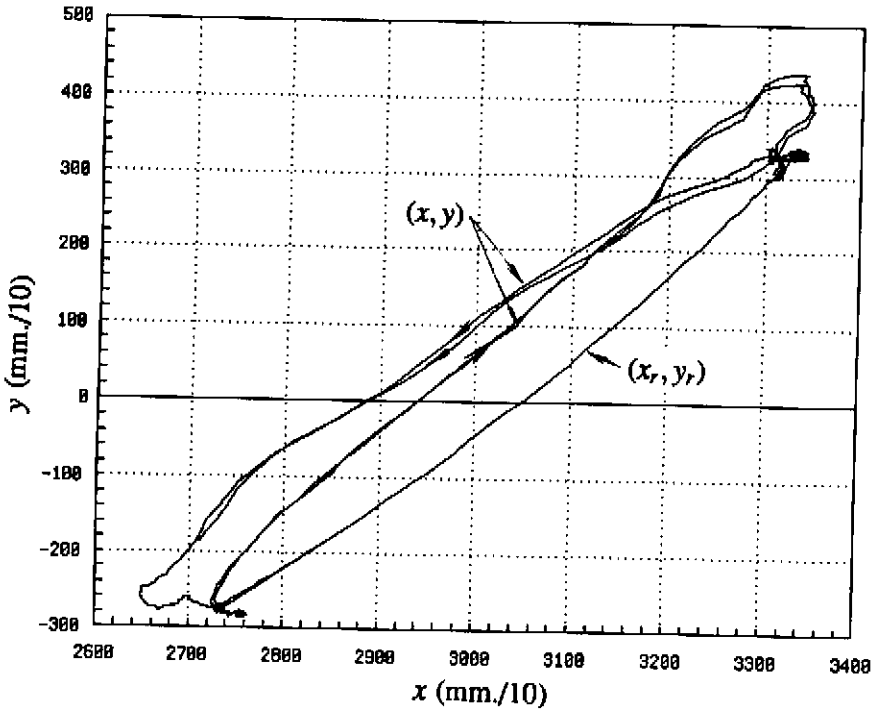

Figure 28: Tip response in cartesian coordinates to a trajectory with the maximum allowable accelerations.

References

[1] Rattan, K.S., Feliu, V., and Brown, H.B.
A Robust Control Scheme for Flexible Arms with Friction in the Joints.
1988 NASA - Air Force Workshop on Space, Operation, Automation and Robotics. Dayton (USA), July, 1988.

[2] Feliu, V., Rattan, K.S and Brown H.B.
A New Approach to Control Single-Link Flexible Arms. Part II: Control of the Tip Position in the Presence of Joint Friction.
CMU-RI-TR-89-14. Technical Report, Robotics Institute, Carnegie Mellon University.
July 1989.

[3] Feliu, V., Rattan K.S. and Brown H.B.
Adaptive Control of a Single-Link Flexible Manipulator in the Presence of Joint Friction and Load Changes.
1989 IEEE International Conference on Robotics and Automation, Scotsdale (USA), May 1989.

[4] Craig, J.J.
Introduction to Robotics. Mechanics & Control. Addison-Wesley Publishing Company, 1986.

[5] Thomson, W.T.
Vibration Theory and Applications. Prentice-Hall, 1965.